

Optimal surface segmentation using flow lines to quantify airway abnormalities in chronic obstructive pulmonary disease

Jens Petersen^{a,*}, Mads Nielsen^a, Pechin Lo^{a,b}, Lars H. Nordenmark^c, Jesper Holst Pedersen^d, Mathilde Marie Winkler Wille^f, Asger Dirksen^f, Marleen de Bruijne^{a,e}

^aImage Group, Department of Computer Science, University of Copenhagen, Denmark

^bThoracic Imaging Research Group, University of California, Los Angeles, California, United States of America

^cAstraZeneca R&D, Mölndal, Sweden

^dDepartment of Thoracic Surgery RT, Rigshospitalet, University of Copenhagen, Denmark

^eBiomedical Imaging Group Rotterdam, Departments of Radiology & Medical Informatics, Erasmus MC, Rotterdam, The Netherlands

^fDepartment of Respiratory Medicine, Gentofte Hospital, Denmark

Abstract

This paper introduces a graph construction method for multi-dimensional and multi-surface segmentation problems. Such problems can be solved by searching for the optimal separating surfaces given the space of graph columns defined by an initial coarse surface. Conventional straight graph columns are not well suited for surfaces with high curvature, we therefore propose to derive columns from properly generated, non-intersecting flow lines. This guarantees solutions that do not self-intersect.

The method is applied to segment human airway walls in computed tomography images in three-dimensions. Phantom measurements show that the inner and outer radii are estimated with sub-voxel accuracy. Two-dimensional manually annotated cross-sectional images were used to compare the results with those of another recently published graph based method. The proposed approach had an average overlap of $89.3 \pm 5.8 \%$, and was on average within 0.096 ± 0.097 mm of the manually annotated surfaces, which is significantly better than what the previously published approach achieved. A medical expert visually evaluated 499 randomly extracted cross-sectional images from 499 scans and preferred the proposed approach in 68.5 %, the alternative approach in 11.2 %, and in 20.3 % no method was favoured. Airway abnormality measurements obtained with the method on 490 scan pairs from a lung cancer screening trial correlate significantly with lung function and are reproducible; repeat scan R^2 of measures of the airway lumen diameter and wall area percentage in the airways from generation 0 (trachea) to 5 range from 0.96 to 0.73.

Keywords: segmentation, graph, flow lines, airways, computed tomography

1. Introduction

Optimal net surface methods (Wu and Chen, 2002) have seen a growing use within medical image segmentation in the last couple of years, likely due to their ability to find the globally optimal solution of multiple interacting surfaces in multiple dimensions given surface cost functions and a useful range of geometric constraints and penalties in polynomial time using minimum cut algorithms (Li et al., 2006; Liu et al., 2012; Petersen et al., 2010; Yin et al., 2009; Abramoff et al.,

2008; Petersen et al., 2011b; Arias et al., 2012; Kainmueller et al., 2013). In order to use these methods, the segmentation problem needs to be transformed from the space defined by the image voxel grid to some graph representation defined by a set of columns. Each column is associated with a point on the sought surface and represents the set of possible solutions, or positions, the surface can take. A suitable graph should be able to represent all plausible solutions in the image space. For instance, if a graph column does not cross the sought surface or if it crosses it multiple times, then this surface can not be represented by the graph. Similarly, admissible solutions in the space defined by the graph representation should represent valid surfaces in image space, that is, the graph space should for instance not

*Corresponding author

Email addresses: phup@diku.dk (Jens Petersen), marleen@diku.dk (Marleen de Bruijne)

allow self-intersecting surfaces. It is also important that the graph structure allows for a meaningful representation of the surface cost functions and geometric constraints and penalties. Surface non-smoothness can, for instance be reduced, by increasing the cost of solutions in proportion to how much they vary in neighbouring columns. However this is only meaningful if the relative variation within the columns is somehow related to the associated relative variation within image space.

In some cases the sought surfaces are expected to be oriented along an image axis and the voxel columns of the image itself may be used. This has for instance been used in the case of the intraretinal layers in macular optical coherence tomography images (Abràmoff et al., 2008). Other approaches have used simple mathematical transformations, such as those of Li et al. (2006) and Petersen et al. (2010), in which images of tubular airway segments were unfolded using polar transforms in two or three-dimensions. The graph columns were oriented perpendicular to the resulting contours or terrain like surfaces allowing for an easy representation of surface smoothness constraints and penalties. In many cases, however, the surfaces are much too complicated for such an approach and/or the prior knowledge of the surfaces' shape and position required is not available. In these cases such prior knowledge may be gained by employing an initial method to roughly estimate the position of the surfaces and then use an optimal surface graph to refine this estimate. This was done in Liu et al. (2012) by placing columns at points of the initial surface and oriented along the surface normals inward and outward. Problems with intersecting columns and thus self-intersecting surfaces were avoided, by limiting the length of each column to the minimum distance to the initial surface inner and outer medial axes. This approach can result in columns that are too short to reach the desired solution, as shown in Figure 1(a). Yin et al. (2009) suggested columns inspired by the non-intersecting property of electric lines of force. The columns were constructed by simulating electrical charges at surface points of the initial segmentation and tracing the electric lines of force within the field inward and outward. This method is computationally infeasible for large scale problems, as every surface point charge influences the computation of every electric line of force. Furthermore the electric lines of force can behave erratically if the initial segmentation contains small scale errors or noise. Recently Kainmueller et al. (2013) proposed to use omnidirectional displacements, which allow each initial surface mesh vertex to move to uniformly distributed positions within a ball shaped region around it. Self-intersections are

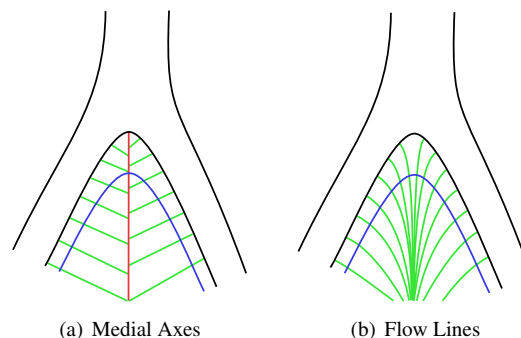


Figure 1: Figure 1(a) illustrates the fish-bone like structure of surface normal direction columns (*green*) based on the distance to the medial axis (*red*) in areas where the initial segmentation (*black*) has high curvature. Notice that the four inner-most columns do not cross the sought surface border (*blue*), which means that the desired solution can not be represented by the graph and the segmented surface will be wrong in these positions. Figure 1(b) shows the advantage of columns based on flow lines (*green*), notice that all columns cross the sought surface.

minimized by using regularisation and the solution is found using Markov Random Field energy minimization. The approach is too computationally expensive for larger problems and so Kainmueller et al. (2013) also shows how it can be combined with an optimal surface - unidirectional column type approach. This makes the method practical for larger problems by using omnidirectional displacements in high curvature regions and unidirectional columns in low curvature regions. The two problems are solved sequentially and so the method does not guarantee global optimality.

In Petersen et al. (2011b) we proposed to use graph columns defined from flow lines within a regularized version of the initial segmentation. Flow lines are non-intersecting and are uniquely defined if the regularisation is smooth, and noise and small errors in the segmentation are naturally dealt with by the same regularisation. Moreover, fast approximations can be computed using image convolution. Figure 1(b) illustrates the concept. The method was originally applied to the problem of segmenting human airway walls in CT images and has since then been used for segmenting the carotid artery bifurcation in magnetic resonance imaging (Arias et al., 2012).

Assessing the dimensions of the airway walls is important in the study of airway remodelling diseases such as Chronic Obstructive Pulmonary Disease (COPD) (Hackx et al., 2012). It is a dual surface problem, consisting of an inner and an outer wall surface, where bifurcations form regions of high curvature that would cause problems for conventional graph construction

approaches. The vast majority of previous airway wall segmentation methods have been one- or two-dimensional in nature. The one-dimensional techniques work by casting rays from the centre of the airways outwards looking for the wall surfaces using the full width at half maximum edge detection principle (Nakano et al., 2000), by phase congruency (Estépar et al., 2006), or more complex models of the scanning point spread function (Weinheimer et al., 2008). The airway wall surfaces resemble concentric circles when seen in a cross-sectional view centred on and perpendicular to the airway centreline. This is what two-dimensional methods typically exploit to impose some degree of regularity on the solution (Petersen et al., 2010; Saragaglia et al., 2006). Three-dimensional methods, however, may use more of the information present in the image, allowing surfaces to be found more accurately when they are close to other structures such as blood vessels. Moreover, bifurcation and carina regions, which typically cannot be segmented with previous two-dimensional approaches, can be analysed (Liu et al., 2012). Besides the already mentioned methods of Liu et al. (2012); Petersen et al. (2011b), a three-dimensional method is also described in Saragaglia et al. (2006), which evolves a deformable mesh, constructed from an initial segmentation of the lumen. The evolution is done with force constraints computed from intensity and gradient magnitude values; elastic forces penalizing local wall thickness variations; and regularisation forces, locally smoothing the result. The method does not guarantee a global optimal solution and unlike the approaches of Liu et al. (2012); Petersen et al. (2011b) the two surfaces are not estimated simultaneously, and thus the added knowledge of the position of the exterior surface is not used to improve the inner surface. Ortner et al. (2010) also proposed to use a deformable mesh. Their mesh is built from an initial segmentation of the lumen and its evolution is governed by gradient vector flow and simplified Lagrangian dynamics and so avoids self-intersections. The approach was evaluated on simulated CT data and 15 clinical cases of mild and severe asthmatics, showing good agreement with segmentation result and clinical expertise.

This paper is an extension of the work presented in Petersen et al. (2011b). The main differences are the addition of a constraint, that forces the outer surface to be outside the inner; improvements in the parameter tuning, such that all involved parameters are automatically estimated using a manually annotated training set; adjustment of parameters and evaluation of results according to the COPDGene phantom (Sieren et al., 2012) to account for a possible bias present in the manual anno-

tations; and finally the addition of an extensive medical expert visual evaluation comparing the result of the proposed approach with that of Liu et al. (2012). We show that the method can be used to measure airway abnormalities associated with COPD reproducibly.

2. Methods

2.1. Initial Segmentation

We will assume the existence of a coarse initial segmentation, a single object given by the voxels in the set S , whose surface should be roughly similar to the surfaces we are looking for. For our application we used an airway tree extraction algorithm based on Lo et al. (2009), which returns a three-dimensional binary segmentation of the airway lumen.

The initial segmentation needs to be converted to a mesh. To this end, we used vertices at the centre of each surface voxel face and the neighbourhood given by the face edge neighbours, such that each vertex has 4 neighbours. We will denote the vertices in this mesh with \mathcal{V} , and represent the neighbourhood with an edge set \mathcal{E} , where $(i, j) \in \mathcal{E}$ denotes that the vertices $i, j \in \mathcal{V}$ are neighbours.

2.2. Flow Lines

The graph will be defined from flow lines at each of the mesh vertices. A flow line in a vector field is tangent to the field at each point, and if the field is defined as the gradient field of a scalar potential ϕ , it will follow the direction with the greatest rate of change of this potential. Electric lines of force are examples of flow lines in an electric field and interestingly the magnitude of the electric field can be formulated as a convolution operation. The approach of Yin et al. (2009) can thus be efficiently approximated using fast convolution algorithms. Rather than being limited to electric fields, we propose, however, to use the more general case of flow lines based on scalar potentials defined by the convolution:

$$\phi(\mathbf{x}) = \int \mathbf{1}_S(\hat{\mathbf{x}})R(\hat{\mathbf{x}} - \mathbf{x})d\hat{\mathbf{x}}, \quad (1)$$

here \mathbf{x} is the position to be evaluated and $\mathbf{1}_S$ is the indicator function for the initial segmentation S .

In this work we experimented with generating the potentials from two different types of filters. The first can be considered a regularised electric line of force approach:

$$R(\mathbf{x}) = \frac{1}{\alpha + |\mathbf{x}|^2}, \quad (2)$$

where $\alpha > 0$ is the regularisation constant, which makes R well defined for all \mathbf{x} . This regularisation has the added effect of smoothing the result, which is useful if the initial segmentation contains noise. When $\alpha \rightarrow 0$, ϕ becomes proportional to the magnitude of the electric field at \mathbf{x} arising from a continuous 'charge density' given by $\mathbf{1}_S$. This option is therefore similar to the method introduced in Yin et al. (2009). However, rather than using a discrete set of surface point 'charges', which introduce local singularities, ϕ is defined everywhere and thus allow us to trace the flow lines consistently through the initial surface. The second filter is given by the Gaussian kernel, which offers more regularisation and more locality because of its faster decaying tails:

$$R(\mathbf{x}) = ce^{-|\mathbf{x}|^2/(2\sigma^2)}. \quad (3)$$

The flow lines $\varphi_i : \mathbb{R} \rightarrow \mathbb{R}^n, i \in \mathcal{V}$ are found as the solution to the following ordinary differential equation:

$$\frac{\partial \varphi_i}{\partial t}(t) = \nabla \phi(\varphi_i(t)) \quad (4)$$

with initial value $\varphi_i(0) = i$. An implementation (Galassi et al.) of the Runge-Kutta-Fehlberg method (Fehlberg, 1970) was used to approximate the solutions. At some point the gradient flattens such that the flow line can no longer be traced due to numerical issues or the limited support of the employed discrete convolution kernel, resulting in a column with a finite number of inner and outer column points relative to i .

With no approximations the running time of computing electric lines of force as suggested in Yin et al. (2009) is given by $O(\eta \times |V|^2)$, where η is the number of times the gradient needs to be computed to trace each electric line of force. This is because the charge at each of the mesh vertices influences the computation of the gradient needed to compute the electric line of force at each of the other mesh vertices. However using discrete convolution, an approximated gradient can be computed efficiently and represented as an image. Computing the gradient in an arbitrary position is then a matter of simple interpolation, and the running time of computing flow lines as suggested in this work is thus $O(\eta \times |V|)$.

2.3. Graph construction

This section describes how an optimal surface graph $G = (V, E)$ with vertices V and edges E can be constructed, such that the minimum cut of G defines the sought surfaces.

We will use the term *penalty* to describe what could be called a soft constraint, that is, something that has

the effect of increasing the cost and decreasing the likelihood of a given solution. A *constraint* on the other hand refers to a condition the solution is required to satisfy.

The vertices V of the graph G are arranged in columns $V_i^m = \{i_k^m \mid k \in K_i\}$, one for each vertex $i \in \mathcal{V}$ of the initial surface mesh and for each sought surface $m \in M$, plus source s and sink t vertices. $K_i = \{-I_i, 1 - I_i, \dots, 0, \dots, O_i\}$ denote the indices associated with the sampled flow line with I_i and O_i inner and outer column points relative to i . In this way, the columns associated with each sought surface are corresponding, that is, they represent the same set of possible positions, given by the sampled flow lines. We therefore have:

$$V = \bigcup_{i \in \mathcal{V}, m \in M} V_i^m \cup \{s, t\}. \quad (5)$$

In the case of airway wall segmentation, $M = \{0, 1\}$ would denote the fact that there is an inner and outer surface sub-graph.

Let $w_i^m(k) \geq 0$ denote the surface cost function or the data term of the optimization problem, which maps a vertex with index $k \in K_i$ in a column V_i^m to the cost of making this vertex part of the surface m , see Section 2.4. Also let $f_{i^m, j^n}(|k - l|)$ be a convex non-decreasing function describing the pairwise cost (or penalty) of vertices $i_k^m \in V_i^m$ and $j_l^n \in V_j^n$ being part of the solution of the surfaces $m, n \in M$ respectively. These pairwise penalties are used to implement surface smoothness and separation penalties, see Equation (8). The vertices defining the sought surfaces $\mathcal{N} \subseteq V$, are then a solution to the following minimization problem:

$$\begin{aligned} \mathcal{N} = \arg \min_{\hat{\mathcal{N}} \subseteq V} & \sum_{i_k^m \in \hat{\mathcal{N}}} w_i^m(k) + \sum_{i_k^m, j_l^n \in \hat{\mathcal{N}}} f_{i^m, j^n}(|k - l|) \\ \text{s.t. } & \exists! k(i_k^m \in \hat{\mathcal{N}}) \\ & i_k^m, j_l^n \in \hat{\mathcal{N}} \Rightarrow l \in \Omega(i_k^m, j_l^n), \end{aligned} \quad (6)$$

The first of the constraints ($\exists! k(i_k^m \in \hat{\mathcal{N}})$) ensures that one and only one vertex in each column is part of the solution. This is a needed requirement for the method to work, and it also has the effect that the topology of the initial segmentation is preserved in the solution surfaces. The second constraint ($i_k^m, j_l^n \in \hat{\mathcal{N}} \Rightarrow l \in \Omega(i_k^m, j_l^n)$) enforces pairwise limits on which vertices can be included, by using the set $\Omega(i_k^m, j_l^n) = \{l', l' + 1, \dots, l' + \delta\} \subseteq \{-I_j, 1 - I_j, \dots, O_j\}$. That is, if some vertex i_k^m is part of the solution \mathcal{N} , then the solution must include one of the vertices in $j_{l'}, j_{l'+1}, \dots, j_{l'+\delta}$ as well.

In our experiments we define the data term based on image derivatives, as explained in detail in Section 2.4.

We used the following edge constraints to force the outer surface to be outside the inner:

$$\Omega(i_k^m, j^n) = \begin{cases} \{k, k+1, \dots, O_j\} & \text{if } m=0 \text{ and } n=1 \\ K_j & \text{otherwise.} \end{cases} \quad (7)$$

The following pairwise penalty functions were implemented:

$$f_{i^m, j^n}(x) = \begin{cases} p_m x & \text{if } m=n \text{ and } (i, j) \in \mathcal{E} \\ qx & \text{if } m \neq n \text{ and } i=j \\ 0 & \text{otherwise,} \end{cases} \quad (8)$$

where \mathcal{E} is the neighbourhood defined in Section 2.1, p_m is the smoothness penalty, defining the cost of each index the solution varies between neighbouring columns in the same surface m , and q is the separation penalty, defining the cost for each index the surfaces are separated in each column.

Next we will describe how to construct the edge set E , such that the solution given by a minimum s - t cut in G satisfies Equation 6. It should be noted that our construction differs from previous methods (Ishikawa, 2003; Wu and Chen, 2002), in its ability to deal with columns of varying inner and outer length. First we will note that the edges of E are directed and are associated with a capacity and we will use the following notation ($v \xrightarrow{c} u$), to indicate an edge from vertex v to vertex u with capacity c . We will also remind the reader that an s - t cut in a graph is a partition of the vertices of the graph into two disjoint subsets such that s and t belong to different subsets. The cost of the s - t cut, is the sum of the capacities of the edges going from the source-set (the specific subset s belongs to) to the sink set (the specific subset t belongs to). The vertices in the sought surfaces \mathcal{N} will be given by the vertex $i_k^m \in V$ in each column, which has the highest index k and is part of the source-set.

The data term can be implemented with the following edges:

$$E_d = \left\{ (i_k^m \xrightarrow{w_i^{(k)}} i_{k+1}^m) \mid i_k^m, i_{k+1}^m \in V \right\} \cup \left\{ (i_{O_i}^m \xrightarrow{w_i^{(O_i)}} t), (s \xrightarrow{\infty} i_i^m) \mid i_{O_i}^m, i_i^m \in V \right\}. \quad (9)$$

Since each column is a direct line of flow from the source to the sink, it will always be cut at least once. However in some degenerate cases, multiple cuts might exist in each column violating the first constraint of Equation 6. To prevent this, infinite cost edges directed opposite to the data term edges are added:

$$E_\infty = \left\{ (i_k^m \xrightarrow{\infty} i_{k-1}^m) \mid i_{k-1}^m, i_k^m \in V \right\}. \quad (10)$$

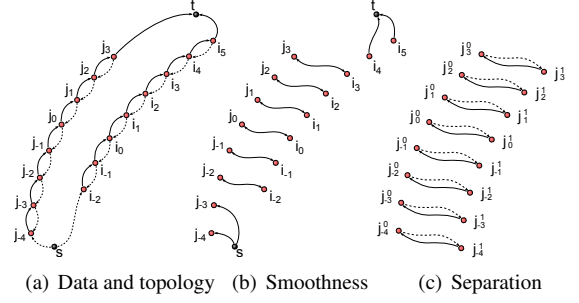


Figure 2: Two neighbouring columns V_i and V_j showing the graph construction as implemented in this paper. These columns have $I_i = 2$ and $I_j = 4$ inner column vertices and $O_i = 5$ and $O_j = 3$ outer column points (note m subscript left out for clarity in 2(a) and 2(b)). The dotted edges have infinite capacity and implement the topology (2(a)) and separation constraints (2(c)). The solid edges have capacities as determined by the data term (2(a)), smoothness (2(b)) and separation penalty (2(c)). Here $L(j, i) = \{-4, -3\}$, $U(i, j) = \{4, 5\}$, and $L(i, j) = U(j, i) = \{\}$.

An example of these edges is given in Figure 2(a).

The edge penalties and constraints can be implemented by the following edges:

$$E_i = \left\{ (i_k^m \xrightarrow{\Delta(i_k^m, j_l^n)} j_l^n) \mid k \in K_i, l \in K_j \right\} \cup \left\{ (s \xrightarrow{\Delta(i_k^m, j_l^n)} j_l^n) \mid l \in K_j, k \in L(j, i) \right\} \cup \left\{ (i_k^m \xrightarrow{\Delta(i_k^m, j_l^n)} t) \mid k \in K_i, l \in U(i, j) \mid i, j \in \mathcal{V}, m, n \in M \right\}, \quad (11)$$

where L and U are the needed lower and upper edge endpoints, which are missing due to differences in column inner and outer lengths, see Figure 2 for an example:

$$\begin{aligned} L(i, j) &= \{k \mid k \in K_i, k < -I_j\} \\ U(i, j) &= \{k \mid k \in K_i, k > O_j\}, \end{aligned} \quad (12)$$

and Δ is the capacity of the edges calculated from the pairwise penalty function:

$$\Delta(i_k^m, j_l^n) = \begin{cases} \infty & \text{if } l = \min \Omega(i_k^m, j_l^n) \\ 0 & \text{if } l \notin \Omega(i_k^m, j_l^n) \\ \hat{\Delta}_{i^m, j^n}(k-l) & \text{otherwise} \end{cases} \quad (13)$$

where

$$\hat{\Delta}_{i^m, j^n}(x) = \begin{cases} 0 & \text{if } x < 0 \\ f_{i^m, j^n}^m(1) - f_{i^m, j^n}^m(0) & \text{if } x = 0 \\ f_{i^m, j^n}^m(x+1) - 2f_{i^m, j^n}^m(x) + f_{i^m, j^n}^m(x-1) & \text{if } x > 0, \end{cases} \quad (14)$$

ensures that any solution will include the cost of the pairwise penalties. For a proof of why this is so refer to Wu and Chen (2002). Notice that $\Delta(i_k^m, j_l^m) \geq 0$ for all $i_k^m, j_l^m \in V$, so the edge capacities are all positive.

Note there is a computational advantage of using the linear pairwise penalty functions of Equation 8 compared to non-linear pairwise penalty functions, as far fewer edges are needed to implement them because $\hat{\Delta}_{i_k^m, j_l^m}(x) = 0$ for all $x \neq 0$. An illustration of these edges is given in Figure 2(b) and 2(c).

The total edge set E in the maximum flow graph is given by:

$$E = E_d \cup E_\infty \cup E_i. \quad (15)$$

We used the algorithm described in Boykov and Kolmogorov (2004) to find the minimum cut.

2.4. Data Term

In this section we describe how the data term part of Equation 9 was implemented for the airway wall segmentation problem. The columns, in this case, will usually start inside the air-filled lumen area, which has low density, move through the airway wall where the density rises, and finally end up in the lung parenchyma where the density falls again. The CT intensity directly reflects this density change. A common way to find such boundaries is to use weightings of the first and second order derivatives of the intensity along the columns (Li et al., 2006; Liu et al., 2012; Petersen et al., 2010). Because the extrema of the second order derivative are slightly shifted and on opposite sides of the first order derivative weighting the derivatives allows one to adjust the position of the found surface according to some known ground truth. In this way one can adjust for bias introduced by partial volume effects:

$$\hat{w}_i^0(t) = \begin{cases} (1 - |\gamma_0|)d_i(t) + \gamma_0 \frac{\partial d_i(t)}{\partial t} & \text{if } d_i(t) > 0 \\ 0 & \text{otherwise} \end{cases}, \quad (16)$$

$$\hat{w}_i^1(t) = \begin{cases} (|\gamma_1| - 1)d_i(t) + \gamma_1 \frac{\partial d_i(t)}{\partial t} & \text{if } d_i(t) < 0 \\ 0 & \text{otherwise} \end{cases}, \quad (17)$$

where $\gamma_0, \gamma_1 \in [-1, 1]$ are the weights, $d_i(t) = \frac{\partial I \circ \varphi_i}{\partial t}(t)$, is the first order derivative of the image intensity I along the flow line φ_i . To get the actual cost functions, the functions are inverted:

$$w_i^m(k) = \max_{j \in \mathcal{V}, l \in \mathcal{K}_j} \hat{w}_j^m(j_l^m) - \hat{w}_i^m(i_k^m). \quad (18)$$

Numerically we approximate the derivatives using central differences from cubically interpolated values.

3. Experiments

Experiments were conducted with three methods based on different ways of constructing the columns. One was a method using straight columns $S_{k,\tau}$, as described in Liu et al. (2012), where the medial axes and normals were determined using the method of Dey and Sun (2006) using k neighbours and an error tolerance of τ respectively. We refer to the original article for a definition of these parameters. The other two methods used the proposed flow line columns calculated using convolution kernels based on Equation 2 and using a Gaussian of scale σ , denoted F_α and F_σ respectively. The resolution of the initial mesh used in the experiments was $0.5 \text{ mm} \times 0.5 \text{ mm} \times 0.5 \text{ mm}$ and the flow lines were sampled at 0.5 mm arc length intervals.

3.1. Data

The material used comes from the Danish Lung Cancer Screening Trial (DLCST) (Pedersen et al., 2009). The images were obtained using a Multi Detector CT scanner (16 rows Philips Mx 8000) with a low dose (120 kV and 40 mAs), and reconstructed using a hard kernel (D) with a resolution of approximately $0.78 \text{ mm} \times 0.78 \text{ mm} \times 1 \text{ mm}$.

Lung function measurements were performed according to recommendations by the European Respiratory Society (Miller et al., 2005) using a computerized system (Spirotrac IV; Vitalograph, Buckingham, UK). No bronchodilation was applied.

As in Petersen et al. (2011b) we use a randomly selected training and test set of 8 and 7 images for parameter tuning and evaluation. From the test and training data set we extracted 329 and 319 two-dimensional cross-sectional sub-images with a resolution of $0.5 \text{ mm} \times 0.5 \text{ mm}$ at random positions perpendicular to and centred on the airways. We then manually annotated these images with lumen M_l and complete airway M_a area. Some of the sub-images contain regions, which we will denote X , which belong to other airway branches. As the orientation of these other branches is unknown annotation may be difficult, and they were therefore marked and excluded from the analysis. The COPDGene phantom (Sieren et al., 2012) was scanned with the DLCST protocol and the 6 airway-like tubes present in the phantom were used to further adjust method parameters and validate segmentation accuracy. Additionally we randomly selected 499 subjects for the medical expert visual comparison. 490 of these had repeated scans and spirometry within a two year period and were further selected to evaluate reproducibility of

measures of airway morphology as well as their correlation with lung function. Of these, 266 are men and 270 were found to be asymptomatic at first scan time, 143, 71 and 6 had COPD stage 1, 2 and 3 respectively according to the criteria of the global initiative for chronic obstructive lung disease (Rabe et al., 2007). The average scan interval was 432 ± 32 days. The average absolute interval between scan and lung function measurement was 12 days.

3.2. Parameter tuning

The methods have inner and outer smoothness penalties, inner and outer cost function derivative weightings and separation penalties, denoted p_m, γ_m and q where $m \in \{0, 1\}$ respectively, plus the method specific parameters, that is k, τ (Section 3) and α and σ (Section 2.2). Optimal values of all these parameters were obtained by searching the parameter space on the training data set using an iterative algorithm. In each iteration, a parameter is searched by probing upper and lower search interval limits. If no improvement is detected in the average value of the error metric Φ , see Section 3.3, over all subjects in the training set, the intervals are halved around the current best guess and the process is repeated. This continues until a better guess is found or the difference between the upper and lower search intervals becomes less than a threshold. The search then proceeds with the next parameter in a loop with reset upper and lower search interval limits until no more parameters get updated. In order to avoid getting stuck in a local minimum, the algorithm was repeated 10 times using random values as initial guesses for the parameters.

3.3. Comparison with manual annotations

We evaluate the correctness of a segmentation in the cross-sections using the relative area of overlap outside the excluded area, Φ as follows:

$$\Phi(M_l, M_a, A_l, A_a, X) = \frac{\frac{|(M_l \cap A_l) \setminus X|}{|M_l \setminus X| + |A_l \setminus X|} + \frac{|(M_a \cap A_a) \setminus X|}{|M_a \setminus X| + |A_a \setminus X|}}{2}, \quad (19)$$

where A_l and A_a denote lumen and complete airway area as found by the algorithms.

Define the contour $C(A)$ of an area A as the set of pixel centres belonging to A , where at least one of the pixels in the standard 4-neighbourhood is not part of A . The average contour distance was then defined by:

$$\Psi(M_l, M_a, A_l, A_a, X) = \frac{\text{mean}_{x \in C(A_l \setminus X)} d(C(M_l \setminus X), x)/2 + \text{mean}_{x \in C(A_a \setminus X)} d(C(M_a \setminus X), x)/2}{2}, \quad (20)$$

where $d(A, x)$ defines the minimum euclidean distance between the point x and the set A . Note, that this validation is performed in resampled images of the resolution of the graph, which is higher than the original image resolution.

3.4. Phantom experiments

It has been established that humans tend to underestimate the lumen and overestimate the wall area (King et al., 2000) and graph segmentations tuned to manual segmentations are likely to be biased in the same manner. We therefore conducted a second round of tuning of the data term parameters γ_0 and γ_1 of all the methods involving the COPDGene phantom as ground truth. The airway-like tubes of the phantom were initially segmented using a region growing approach with an upper threshold of -900 HU. The unsigned relative deviation of the inner and outer radii on each tube was used as an error metric both to tune the parameters and to evaluate segmentation performance.

3.5. Observer study

As a final comparison between F_σ and $S_{k,\tau}$ we let a medical expert (MMWW) judge the quality of the segmentations using the phantom tuned parameters. For each subject in the data set a single random position in the airway tree was selected. In this position three cross-sectional images were extracted perpendicular to the centreline. One image containing the original scan data and the other two the original scan data overlaid with the segmentation results of the two methods. We automatically removed all segmented components not connected to the centre-most pixel, to restrict evaluation to the part of the airway viewed perpendicularly. The medical expert was presented with these three images in one view and was asked to decide among four options: 1) result of method a is best, 2) result of method b is best, 3) both results are of equal quality, or 4) not enough information is present to make the decision. The expert could scroll through the scans of the data at will, but was blinded to which method created them. When moving to the next scan, the position of the segmented images in the view would switch randomly. Figure 5 column 1, 3 and 4 illustrate how these images look.

It should be noted that F_α was not included in this final comparison as we thought it would complicate matters unnecessary to have the medical expert choose between three methods of which two were our own. We therefore did the comparison with the variation of our method which performed the best on the manual annotations (Section 4.1).

Method	$S_{k,\tau}$	F_α	F_σ
p_0	125	30	48
p_1	194	213	23
γ_0	-0.36	-0.34	-0.41
γ_1	-0.43	-0.31	-0.57
q	5.2	6.2	6.8

Table 1: Optimal parameters obtained using the training set and phantom. In addition k , τ , α , and σ were estimated to be 103, 4.6, 0.03, and 0.50.

3.6. Reproducibility and correlation with lung function

Airway centrelines and branch generations were extracted from the airway tree with a front propagation method, as described in Lo et al. (2012). Airway morphology was quantified using Lumen Diameter (LD) and Wall Area percentage (WA%) computed from distances of the inner and outer surfaces to the nearest point on the centreline. Measurements were averaged by branch generations, with trachea assigned generation zero. We assume that changes in the airways due to disease are relatively minor in the roughly one year period between the repeated scans, and that changes in the measures are mostly due to measurement variability. We quantify the reproducibility of the measures, with the coefficient of determination, calculated from Pearson product moment correlation coefficients.

4. Results

Table 1 shows optimal parameters obtained using the training set and phantom as described in Section 3.2 and 3.4.

Figure 3 illustrates the effect of the different column construction approaches on what constitutes "smooth" solutions in terms of the implemented penalties. It also illustrates the issues $S_{k,\tau}$ has with shorter columns in high curvature areas.

Running the methods on an image from our data usually takes less than 5 minutes (On a 1.6 GHz laptop using no parallelisation) using up to 4 GB of memory. Figure 4 shows a visualization of a three-dimensional segmentation result of F_σ and Figure 5 shows cross-sections illustrating results of the investigated methods.

4.1. Comparison with manual annotations

Table 2 shows the results of the comparisons with the manual annotations in the test data set, for each of the investigated methods using the optimal parameters. All methods performed well; no method had an average relative area of overlap of less than 0.871 and a maximum

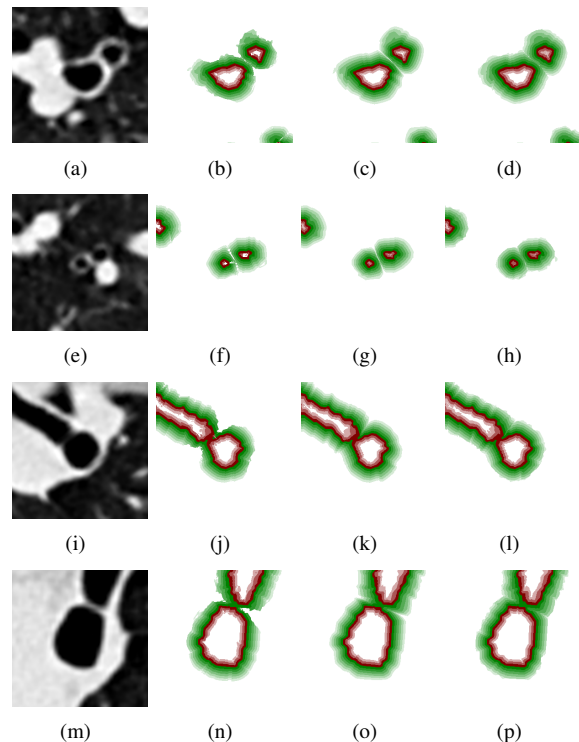


Figure 3: Identically coloured pixels illustrate solutions with zero smoothness penalty at different column indices. The outer-most red surface is the initial segmentation surface. The first column of images is the original scan, the next are of the $S_{k,\tau}$, F_α , and F_σ methods respectively. $S_{k,\tau}$ is most notably different from the flow line approaches in the high curvature areas, where a decreased smoothness can be observed, likely due to shorter columns. The surfaces of F_σ are different from F_α due to an increased local regularisation with limited long range effects, which is especially apparent in the bifurcation regions, where the surfaces of the two branches join earlier.

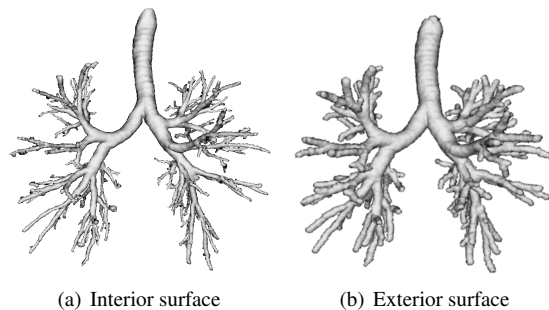


Figure 4: Three-dimensional visualizations of an inner and outer surface extracted by F_σ .

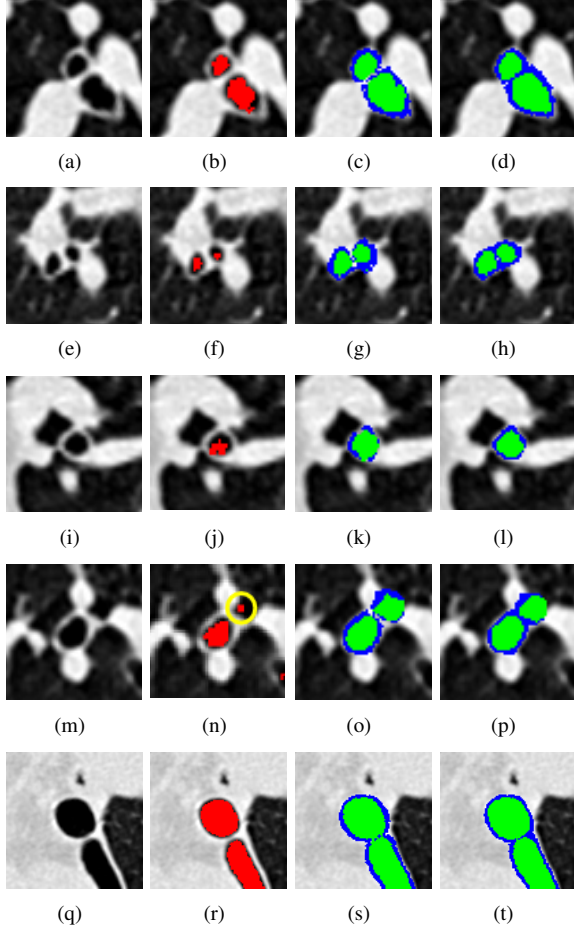


Figure 5: The first column of images from the left shows cross-sections extracted perpendicular to the centre-most airway centreline. The rest towards the right show the same but overlaid with the initial segmentation and the segmentations of $S_{k,\tau}$ and F_σ respectively. Only the lumen (green) and wall (blue) segmentations connected to the centred airway are shown. Notice how the flow line based method does better in the region with high curvature between the bifurcating airway branches in 5(d) and 5(h) compared to results of $S_{k,\tau}$ seen in 5(c) and 5(g). Also note the less noisy and more smooth result of F_σ compared to $S_{k,\tau}$ illustrated in the third row, showing how the flow line approach is better able to deal with the relatively poor initial segmentation. The second to last row illustrates how neither of the methods are able to correct larger errors in the initial segmentation, such as the over-segmented area encircled in 5(n). The last row shows a segmentation result near the mediastinum, where the outer border has weak contrast. In such situations the implemented smoothness penalties help find the surface by integrating information from nearby areas where the contrast is stronger.

Method	Φ	Ψ (mm)
$S_{k,\tau}$	0.871 ± 0.075	0.135 ± 0.149
F_α	0.883 ± 0.066	0.110 ± 0.134
F_σ	0.893 ± 0.058	0.096 ± 0.097

Table 2: The results of different methods and kernels on the test data set with 319 manually annotated slices. Mean \pm standard deviation of (19) and (20). The best result marked with a bold font.

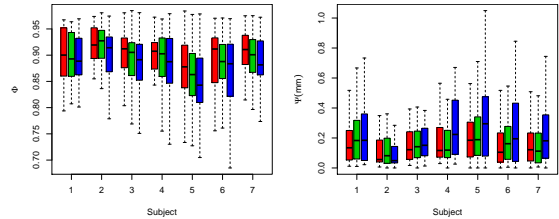


Figure 6: Result on the manually annotated test data set by subject of F_σ (red), F_α (green) and $S_{k,\tau}$ (blue). Bar shows median, box at lower and upper quartiles, and whiskers at interquartile range.

average curve distance of more than 0.135 mm. F_σ achieved the significantly best result ($p < 0.05$) and the smallest variance in the quality of the results ($p < 0.05$) in terms of both metrics, while results of $S_{k,\tau}$ were the worst ($p < 0.001$). Results were compared using a Wilcoxon signed-rank test and a two-sample F -test respectively. It should be noted that these tests assume the samples to be independent, which can be questioned given that multiple cross-sectional slices were selected from each of the scans. However the mean accuracy of F_σ was better than $S_{k,\tau}$ in every single subject and using both metrics, which is significant in itself ($p < 0.05$). Figure 6 shows the results by subject.

4.2. Comparison with phantom

Table 3 shows the results of the phantom segmentation. Interior and exterior radii were estimated to within an average unsigned error of 6.6% (-15.4 % to 7.6 %)

Tube	Interior radius (mm)		Exterior radius (mm)	
	Measured	Actual	Measured	Actual
0	3.23	3	4.14	4.5
1	3.00	3	3.80	3.9
2	1.27	1.5	2.13	2.1
3	1.33	1.5	2.11	2.1
4	3.10	3	3.98	4.2
5	3.07	3	3.94	4.2

Table 3: Measured and actual phantom radii in mm.

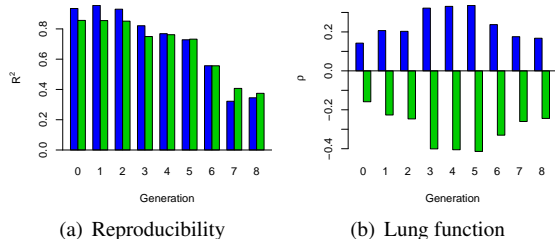


Figure 7: Figure 7(a) shows the reproducibility of the measures, LD (blue) and WA% (green), in repeated scans quantified as R^2 in branch generations 0 to 8. Figure 7(b) shows significant ($p < 0.01$) Spearman correlation coefficients of the same measures with lung function.

and 4.0 % (-8.0 % to 1.5 %) respectively. In absolute terms the radii deviated an unsigned average of 0.13 mm (-0.23 mm to 0.23 mm) and 0.16 mm (-0.36 mm to 0.16 mm) respectively, which is well below the graph resolution used.

4.3. Medical expert observer comparison

Out of the 499 evaluated cases the medical expert judged the flow line approach to be best in 342 cases, which is significantly more than the 56 cases in which the approach of Liu et al. (2012) was judged to be best, with $p < 0.001$ according to a proportion test. In 92 cases results were found to be of equal quality and in 9 cases the expert ruled that not enough information was present to judge.

The distribution of the proportion of cases where the flow line approach was judged to be best with respect to relative position of the cross-section within the branch was investigated to reveal whether the beginning, top 20% of the centreline; ending, bottom 20%; and middle, the rest of the branch was handled better than with the approach of Liu et al. (2012). The observer preferred the proposed approach in significantly more cases in all parts of the branch according to a proportion test ($p < 0.001$), specifically, 71 out of 107 cases (66%) in the beginning, 211 out of 301 cases in the middle (70%) and 60 cases out of 82 in the bottom (73%). The proportions were not significantly related to branch position ($p = 0.59$).

4.4. Airway abnormality measurements

Figure 7(a) shows reproducibility of LD and WA% quantified as repeat scan R^2 . In general both measures have good reproducibility down to generation 5 ($R^2 > 0.73$) and the reproducibility is falling with increasing generation.

Figure 7(b) shows Spearman’s correlation coefficients ρ of the measures and lung function measured by

Forced Expiratory Volume in one second as a percentage of the predicted value (FEV1 (% predicted)). LD is positively correlated, indicating luminal narrowing with COPD, whereas WA% is negatively correlated, indicating wall thickening. Correlation is seen to increase with generation until generation 5.

5. Discussion

In this paper we have shown how optimal net surface graphs based on columns defined from properly generated flow lines can be used to accurately find multiple interacting surfaces in multiple dimensions. Compared to previously used straight columns, the method should be better able to handle high curvature regions and noisy initial segmentations. We have demonstrated how the approach can be used to find the surfaces of the airway walls in CT images. The high reproducibility of the resulting airway abnormality measurements as well as the fact that the measurements show significant correlation between decreased lung function and luminal narrowing and wall thickening, in agreement with the current knowledge of the disease process in COPD, indicate the method can be used to measure abnormalities caused by COPD up to at least generation 5.

We experimented with two different convolution kernels to obtain the flow lines, both giving good results. For our specific application, the Gaussian kernel F_σ performed better than F_α , which we think is mainly due to it tending to zero much faster, limiting long range effects while providing strong regularization near the potentially noisy initial surface. The most suitable kernel and kernel parameters may vary per segmentation task. In cases where one of the true surfaces can be far from the initial segmentation for instance, a kernel with longer tails may be needed.

In this work, we performed an extensive parameter tuning for each of the methods to allow for an as objective comparison as possible. However, it is our experience that results are not very sensitive to the settings of these parameters and suitable settings can already be obtained by a few trial and error runs using visual inspection of the segmentation results.

The graph resolution was set relatively low (0.5 mm), compared to that of Liu et al. (2012) (0.1 mm) to limit computation times and memory consumption. This results in a slightly lower accuracy on phantom scans than what Liu et al. (2012) report, however, there is no reason to doubt if the improvement in accuracy on real data as seen with our approach will carry over to higher graph resolutions as well.

The chosen mesh is not very smooth and so it could be questioned whether the methods perform differently simply because of differences in their ability to deal with this non-smoothness. To explore whether this was the case we repeated the training (Section 3.2) with meshes based on the marching cubes algorithm, as was used in Liu et al. (2012) and a smooth mesh based on Boissonnat and Oudot (2005) and evaluated their results on the test set (Section 3.3). The mesh based on Boissonnat and Oudot (2005) overall performed similar to our mesh, whereas marching cubes performed significantly worse with each of the investigated methods. Moreover the ordering of the methods in terms of results seemed to be preserved. This indicates that our mesh choice is not the cause of the differences. An advantage of our mesh is that each vertex has a constant number of adjacent vertices (four) and the distance to its neighbours varies less than with the tested alternatives. This regularity helps make the graph smoothness penalties work more evenly across the surface.

Estimating both airway wall surfaces simultaneously using the initial lumen surface as a prior, makes sense, as the lumen surface is easier to segment than the outer wall surface. This is because the contrast between the outer wall surface and abutting structures, such as vessels can be very low. In low contrast areas results become more driven by smoothness penalties. If the initial segmentation is not unreasonable, good segmentations can be achieved even in these regions as seen in Figure 5(d), 5(h) and 5(t), however in cases where contrast is low and the initial segmentation is also poor, errors can occur. Examples of this can be seen in Figure 5(l), where the wall area in the vascular contact region seems to be underestimated. Sensitivity to the accuracy of the initial segmentation is however not unique to the proposed approach, as all previously developed three-dimensional airway wall segmentation approaches (Liu et al., 2012; Saragaglia et al., 2006) depend on an initial segmentation and one and two-dimensional methods require an accurate estimation of the centreline (Petersen et al., 2010; Weinheimer et al., 2008; Estépar et al., 2006). The method we used to obtain the initial segmentation is state-of-the-art and has been shown to have very few false positives (Lo et al., 2009). Moreover as the lumen segmentation in general seem to be improved compared to the initial segmentation, it is possible that further improvements could be achieved by multiple iterations of the proposed approach.

Although manual annotations can be biased (King et al., 2000), comparison with them is still a valid way to assess a method's ability to find the airway surfaces in a realistic setting. Manual tracings were used in a similar

fashion in Li et al. (2006) in 39 randomly selected slices outside the bifurcation areas. The unsigned errors were reported to be 0.10 ± 0.11 and 0.12 ± 0.12 mm for the inner and outer surfaces respectively, which is similar to what our approach achieved.

An ability to pick up significant changes in airway dimensions related to disease has, to our knowledge, not been demonstrated by previous fully automatic three-dimensional airway wall segmentation approaches. However, other one and two-dimensional approaches have, and significant correlation have for instance been reported with lung function using the approach of Weinheimer et al. (2008) in Achenbach et al. (2008), using the full width at half maximum principle in Nakano et al. (2000) or with exercise capacity in COPD using the approach of Estépar et al. (2006) in Diaz et al. (2010). One should exercise care in drawing conclusions from comparisons of these studies as there are important differences in patient characteristics, and the number of healthy participants, however, our results are within the range reported by them (WA% coefficients of -0.338 (Nakano et al., 2000) to -0.560 (Achenbach et al., 2008)).

Scan-rescan repeatability of the measures was good, but did decrease from generation 6 and onwards as can be seen in Figure 7(a). A large part of this decline can probably be explained by missing branches in the initial segmentations, leading to different branches contributing to the airway measures per generation at the different time points. Comparing the number of segmented branches to the expected value, assuming a binary tree structure, revealed that almost all the branches were segmented in generation 5 (97%), whereas the number had dropped to about 62% in generation 6. Measurements conducted in corresponding branches, as opposed to generations, might thus still be reproducible after generation 5, as was also seen in Petersen et al. (2011a) where image registration was used to do branch matching and limit measurements to repeatedly found branches. The use of higher dosage and resolution scans would probably also result in a higher number of detected branches and higher accuracy in placing the airway wall borders, due to a better definition of edges in especially the smaller airways. This should further improve reproducibility and correlation with lung function especially beyond generation 5.

We expected to see a higher frequency of cases where the proposed method was found superior in the high curvature areas near the bifurcations. The medical expert visual inspection did show a slightly higher proportion in the ending compared to the top and middle parts of the branches, but the difference was not signif-

icant. The results show the proposed method actually improves many cases outside bifurcations as well. An example is given in Figure 5. This could be due to small errors in the initial segmentation, which make it difficult to obtain good estimates of the normal directions. In such cases increased regularisation may help the flow line approach and even if the flow lines follow the same erroneous directions close to the initial segmentation, as they move away, the directions will be relatively more determined by long range interactions, and thus the errors will be evened out.

6. Conclusions

To conclude, a new graph construction technique applicable to multi-dimensional multi-surface segmentation problems was proposed. The method runs in polynomial time and is able to penalize for non-smoothness and separation of the found surfaces. The results are guaranteed to not self-intersect and are robust in regions with large curvature.

We applied the method to the problem of segmenting human airway walls in CT images based on an initial coarse airway lumen segmentation, and results were shown to be significantly more accurate than those of another recently published graph based method. Phantom dimensions were estimated to sub-voxel resolution, and large scale evaluations on 980 images from a lung cancer screening trial showed both good reproducibility of the obtained airway abnormality measures and a significant correlation with lung function.

Acknowledgements

This work was partly funded by the Netherlands Organisation for Scientific Research (NWO), and AstraZeneca Sweden.

References

- Abramoff, M.D., Kardon, R., Russel, S.R., Wu, X., Sonka, M., 2008. Intraretinal layer segmentation of macular optical coherence tomography images using optimal 3-D graph search. *IEEE Transactions on Medical Imaging* 27, 1495–1505.
- Achenbach, T., Weinheimer, O., Biedermann, A., Schmitt, S., Freudenstein, D., Goutham, E., Kunz, R.P., Buhl, R., Dueber, C., Heussel, C.P., 2008. MDCT assessment of airway wall thickness in COPD patients using a new method: correlations with pulmonary function tests. *Eur Radiol* 18, 2731–2738.
- Arias, A.L., Petersen, J., van Engelen, A., Tang, H., Selwaness, M., Witteman, J.C.M., van der Lugt, A., Niessen, W.J., de Bruijne, M., 2012. Carotid artery wall segmentation by coupled surface graph cuts, in: *MICCAI Medical Computer Vision Workshop 2012*.
- Boissonnat, J.D., Oudot, S., 2005. Provably good sampling and meshing of surfaces. *Graphical Models* 67, 405–451.
- Boykov, Y., Kolmogorov, V., 2004. An experimental comparison of min-cut/max-flow algorithms for energy minimization in vision. *IEEE Trans. Pattern Anal. Mach. Intell.* 26, 1124–1137.
- Dey, T.K., Sun, J., 2006. Normal and feature estimation from noisy point clouds, in: *Proceedings of the 26th International Conference on Foundations of Software Technology and Theoretical Computer Science*, pp. 21–32.
- Diaz, A.A., Bartholmai, B., Estépar, R.S.J., Ross, J., Matsuoka, S., Yamashiro, T., Hatabu, H., Reilly, J.J., Silverman, E.K., Washko, G.R., 2010. Relationship of emphysema and airway disease assessed by CT to exercise capacity in COPD. *Respir Med* 104, 1145–1151.
- Estépar, R.S., Washko, G.G., Silverman, E.K., Reilly, J.J., Kikinis, R., Westin, C.F., 2006. Accurate airway wall estimation using phase congruency, in: *Med Image Comput Assist Interv*, pp. 125–34.
- Fehlberg, E., 1970. Klassische runge-kutta-formeln vierter und niedrigerer ordnung mit schrittweitenkontrolle und ihre anwendung auf wrmeleitungsprobleme. *Computing (Arch. Elektron. Rechnen)* 6, 61–71.
- Galassi, M., Davies, J., Theiler, J., Gough, B., Jungman, G., Alken, P., Booth, M., Rossi, F., . GNU Scientific Library Reference Manual (3rd Ed.). URL: <http://www.gnu.org/software/gsl/>.
- Hackx, M., Bankier, A.A., Gevenois, P.A., 2012. Chronic obstructive pulmonary disease: CT quantification of airways disease. *Radiology* 265, 34–48.
- Ishikawa, H., 2003. Exact optimization for markov random fields with convex priors. *IEEE Trans. Pattern Anal. Mach. Intell.* 25, 1333–1336.
- Kainmueller, D., Lamecker, H., Heller, M.O., Weber, B., Hege, H.C., Zachow, S., 2013. Omnidirectional displacements for deformable surfaces. *Medical Image Analysis* 17, 429–441.
- King, G.G., Müller, N.L., Whittall, K.P., Xiang, Q.S., Paré, P.D., 2000. An analysis algorithm for measuring airway lumen and wall areas from high-resolution computed tomography data. *Am J Respir Crit Care Med* 161(2 Pt 1), 574–80.
- Li, K., Wu, X., Chen, D.Z., Sonka, M., 2006. Optimal surface segmentation in volumetric images - a graph-theoretic approach. *IEEE Trans. Pattern Anal. Mach. Intell.* 28, 119–134.
- Liu, X., Chen, D.Z., Tawhai, M., Wu, X., Hoffman, E., Sonka, M., 2012. Optimal graph search based segmentation of airway tree double surfaces across bifurcations. *IEEE Transactions on Medical Imaging*.
- Lo, P., van Ginneken, B., Reinhardt, J.M., Yavarna, T., de Jong, P.A., Irving, B., Fetita, C., Ortner, M., Pinho, R., Sijbers, J., Feuerstein, M., Fabijanska, A., Bauer, C., Beichel, R., Mendoza, C.S., Wiemker, R., Lee, J., Reeves, A.P., Born, S., Weinheimer, O., van Rikxoort, E.M., Tschirren, J., Mori, K., Odry, B., Naidich, D.P., Hartmann, I., Hoffman, E.A., Prokop, M., Pedersen, J.H., de Bruijne, M., 2012. Extraction of airways from CT (EXACT’09). *IEEE transactions on Medical Imaging* 31, 2093–2107.
- Lo, P., Sporring, J., Pedersen, J.J.H., de Bruijne, M., 2009. Airway tree extraction with locally optimal paths, in: Yang, G.Z., Hawkes, D., Rueckert, D., Noble, A., Taylor, C. (Eds.), *Medical Image Computing and Computer-Assisted Intervention MICCAI 2009*. Springer, volume 5762 of *LNCS*, pp. 51–58.
- Miller, M.R., Crapo, R., Hankinson, J., Brusasco, V., Burgos, F., Casaburi, R., Coates, A., Enright, P., van der Grinten, C.P., Gustafsson, P., Jensen, R., Johnson, D.C., MacIntyre, N., McKay, R., Navajas, D., Pedersen, O.F., Pellegrino, R., Viegi, G., Wanger, J., Force, A.T., 2005. General considerations for lung function testing. *Eur Respir J* 26, 153–61.
- Nakano, Y., Muro, S., Sakai, H., Hirai, T., Chin, K., Tsukino, M.,

- Nishimura, K., Itoh, H., Paré, P.D., Hogg, J.C., Mishima, M., 2000. Computed tomographic measurements of airway dimensions and emphysema in smokers - correlation with lung function. *Am J Respir Crit Care Med* 162, 1102–1108.
- Ortner, M., Fetita, C., Brillet, P.Y., Prêteux, F., Grenier, P., 2010. 3D vector flow guided segmentation of airway wall in msct, in: *Bebis, G., Boyle, R.D., Parvin, B., Koracin, D., Chung, R., Hammoud, R.I., Hussain, M., Tan, K.H., Crawfis, R., Thalmann, D., Kao, D., Avila, L. (Eds.), ISVC (2), Springer. pp. 302–311.*
- Pedersen, J.H., Ashraf, H., Dirksen, A., Bach, K., Hansen, H., Toennesen, P., Thorsen, H., Brodersen, J., Skov, B.G., Døssing, M., Mortensen, J., Richter, K., Clementsen, P., Seersholm, N., 2009. The danish randomized lung cancer CT screening trial—overall design and results of the prevalence round. *J Thorac Oncol* 4, 608–614.
- Petersen, J., Gorbunova, V., Nielsen, M., Dirksen, A., Lo, P., de Bruijne, M., 2011a. Longitudinal analysis of airways using registration, in: *Fourth International Workshop on Pulmonary Image Analysis.*
- Petersen, J., Lo, P., Nielsen, M., , Edula, G., Ashraf, H., Dirksen, A., de Bruijne, M., 2010. Quantitative analysis of airway abnormalities in CT, in: *Karssemeijer, N., Summers, R. (Eds.), Medical Imaging 2010: Computer-Aided Diagnosis. Proceedings of SPIE.*
- Petersen, J., Nielsen, M., Lo, P., Saghir, Z., Dirksen, A., de Bruijne, M., 2011b. Optimal graph based segmentation using flow lines with application to airway wall segmentation, in: *IPMI, pp. 49–60.*
- Rabe, K.F., Hurd, S., Anzueto, A., Barnes, P.J., Buist, S.A., Calverley, P., Fukuchi, Y., Jenkins, C., Rodriguez-Roisin, R., van Weel, C., Zielinski, J., 2007. Global strategy for the diagnosis, management, and prevention of chronic obstructive pulmonary disease: GOLD executive summary. *Am. J. Respir. Crit. Care Med.* 176, 532–555.
- Saragaglia, A., Fetita, C., Prêteux, F., 2006. Assessment of airway remodeling in asthma: Volumetric versus surface quantification approaches, in: *Med Image Comput Assist Interv, pp. 413–20.*
- Sieren, J.P., J. D. Newell, J., Judy, P.F., Lynch, D.A., Chan, K.S., Guo, J., Hoffman, E.A., 2012. Reference standard and statistical model for intersite and temporal comparisons of CT attenuation in a multicenter quantitative lung study. *Med. Phys.* 39.
- Weinheimer, O., Achenbach, T., Bletz, C., Düber, C., Kauczor, H.U., Heussel, C.P., 2008. About objective 3-D analysis of airway geometry in computerized tomography. *IEEE Transactions on Medical Imaging* 27, 64–74.
- Wu, X., Chen, D., 2002. Optimal net surface problems with applications, in: *Widmayer, P., Eidenbenz, S., Triguero, F., Morales, R., Conejo, R., Hennessy, M. (Eds.), Automata, Languages and Programming. Springer. volume 2380 of LNCS, pp. 775–775.*
- Yin, Y., Song, Q., Sonka, M., 2009. Electric field theory motivated graph construction for optimal medical image segmentation, in: *Torsello, A., Escolano, F., Brun, L. (Eds.), Graph-Based Representations in Pattern Recognition. Springer. volume 5534 of LNCS, pp. 334–342.*